Author accepted manuscript

Near-Threshold Electron Transfer in Anion-Nucleobase Clusters: Does the Identity of the Anion Matter?

Rosaria Cercola,[1] Edward Matthews,[1] and Caroline E. H. Dessent[1*]

1 Department of Chemistry, University of York, Heslington, York, YO10 5DD, UK.

*ced5@york.ac.uk

Abstract:

Laser photofragmentation spectroscopy of the I^-·adenine (I^-·A) and $H_2PO_3^-$·adenine ($H_2PO_3^-$·A) clusters has been utilized for the first time across the electron detachment thresholds to explore how the anion identity affects intra-cluster electron transfer. Ionic photofragmentation is weak for both clusters, despite strong photodepletion, revealing that both clusters decay predominantly by electron detachment. The spectra of I^-·A display a prominent dipole-bound excited state in the region of the vertical detachment energy, which relaxes to produce deprotonated adenine. In contrast, photoexcitation of $H_2PO_3^-$·A in the near-threshold region does not access a dipole-bound state, but instead displays photofragmentation properties associated with ultrafast decay of an adenine-localized π-π* transition. Notably, the experimental electron detachment onset of $H_2PO_3^-$·A is around 4.7 eV. This value is substantially reduced compared to the VDE expected for detachment of a simple anion-dipole complex. The lower VDE of $H_2PO_3^-$·A can be traced to initial ionization of the adenine, which is followed by significant rearrangement of a hydrogen atom on the neutral surface. We conclude that these dynamics quench access to a dipole-bound excited state for $H_2PO_3^-$·A. Despite the fact that the excess negative charge is located on $H_2PO_3^-$ in the ground-state cluster, the anion in this cluster does not act as a free electron source to initiate free electron attachment or dissociation in the nucleobase. However, the $H_2PO_3^-$·A cluster represents an important new example of an anionic cluster where ionization occurs from the initial neutral moiety of the cluster, and where photodetachment initiates intra-molecular hydrogen atom transfer.

Keywords:

Nucleobase, Electron Attachment, Photodissociation, Electronic excitation, Gas phase

1. Introduction

Low-energy electron attachment to DNA is a biologically important process, which can result in single- and double-strand cleavage, and also lead to the breakdown of individual nucleobases [1-8]. Such low-energy electrons are produced when either ionizing radiation or high-energy particles pass through biological matter and can hence trigger mutagenic changes [9,10]. Due to the importance of low-energy electron-DNA interactions, a wide number of studies have been carried out to better understand the key molecular-level processes involved. Through this range of theoretical and experimental studies it has been found that both dissociative σ^* phosphate orbitals and unoccupied low-lying π^* orbitals of the nucleobases can be involved in preliminary electron capture prior to the secondary process which involves transient negative ion formation [7,8].

Gas-phase iodide ion-nucleobase clusters have been used in a number of recent experimental studies, to probe low-energy electron-nucleobase coupling in a highly controlled environment [11-15]. In such experiments, the iodide ion is photodetached to produce a 'spectator' iodine atom and a low-energy free electron with a well-defined kinetic energy that can be captured by an adjacent molecule [16-18]. The resulting temporary negative ion dynamics can then be monitored either *via* time-resolved photoelectron spectroscopy or photofragment action spectroscopy [11-18].

We have recently investigated the role played in these experiments by the spectator iodine in a dynamical study of the iodide-uracil complex (I^-·U) [15]. Photoexcitation was found to produce I^- photofragments as well as deprotonated uracil, i.e. $[U\text{-}H]^-$, as a minor photofragmentation channel. Electron production from decay of a transient negative ion was also observed. The production spectra for both photofragment ions displayed two peaks centred at ~4.0 and ~4.8

eV, with the lower-energy band being assigned to a dipole-bound excited state of the complex, while the higher-energy band was primarily assigned to excitation of a π-π* transition localized on the uracil. Crucially, although excited states are quite distinctive in nature, the time-resolved photoelectron imaging (TRPEI) measurements indicated that across both bands, the I^- ion was being produced *via* internal conversion of the initially formed excited states back to the I^-·U electronic ground state followed by I^- evaporation [15].

In this work, we aim to further investigate the role played by the iodide ion in electron transfer excitations of these clusters by directly comparing the laser-induced photodissociation behaviour of I^-·adenine (I^-·A) with $H_2PO_3^-$·adenine ($H_2PO_3^-$·A), *via* laser excitation across the region around and above the electron detachment threshold. The $H_2PO_3^-$ anion has been chosen for this study as it mimics the charge-carrying phosphate chain in the ATP and other nucleotides which have been previously studied in gas-phase photophysics experiments. The I^-·A cluster has been investigated by Neumark and co-workers previously *via* TRPEI [19], although any ionic photofragments that accompany near-threshold photoexcitation were not characterised in that study. Thus, the current work is the first investigation to directly probe the I^-·A photofragment channels.

In the TRPEI study of I^-·A [19], two adenine isomers were observed in the clusters, the biologically relevant A9 isomer and the A3 isomer. Adenine is well-known to exist in fourteen stable isomers, with the amine forms A9, A7 and A3 being lower in energy than the enamine/imine forms [20]. The A9 isomer is computed to be the lowest energy isomer in the gas-phase, while the A7 isomer is stabilized in polar solvents and in polar clusters due to its large dipole moment [20]. A dipole-bound anion of the A9 tautomer has been observed via Rydberg electron transfer, with an associated electron affinity of +12 meV [21]. However, the

dipole-bound anions of the A7 and A3 tautomers have not been observed to date, despite having larger dipole moments than A9 [22]. From a number of experimental and theoretical studies, the valence bound A9 anion is thought to be adiabatically unstable. Indeed, theoretical calculations by Raczynska et al. suggest that only the A3 isomer forms a stable valence anion [23]. Figure 1 illustrates the structures of the key A9, A7 and A3 isomers.

(Figure 1)

2. Methods

UV photodissociation experiments were conducted in a laser-interfaced amaZon SL (Bruker Daltonics) ion-trap mass spectrometer as described in detail elsewhere [24, 25]. The clusters were generated by electrospraying a solution of adenine (1×10^{-4} mol dm^{-3}) mixed with droplets of t-butyl ammonium iodide (1×10^{-2} mol dm^{-3}) or a NaH_2PO_3 solution in deionized water (1×10^{-4} mol dm^{-3}). All chemicals were purchased from Sigma Aldrich and used without further purification.

The $X^{-}\cdot A$ (X = I and H_2PO_3) clusters were mass-selected and isolated in an ion-trap prior to laser irradiation. UV photons were produced by an Nd:YAG (10 Hz, Surelite) pumped OPO (Horizon) laser across the ranges 326 – 234 nm (3.8 – 5.4 eV) and 326- 215 nm (3.8 - 5.8 eV). Scans were conducted using a 1 nm step size. The total absorbance of the clusters is presented as photodepletion (PD), which is calculated as the logarithm of the ratio between the ion intensity of mass-selected $X^{-}\cdot A$ clusters without and with irradiation. Photodepletion is corrected for the average number of photons used to dissociate the clusters, following the expression introduced by Dugourd and co-workers: $\ln(Int_{OFF}/Int_{ON})/(\lambda \cdot P)$ [26]. Here, Int_{ON} and Int_{OFF} are the intensities of the parent clusters with and without irradiation respectively, λ is the

irradiation wavelength and P is the average power of the laser. The photodepletion of the $X^{-}\cdot A$ clusters was averaged at each scanned wavelength. Photofragment production was recorded at each wavelength and corrected for the $X^{-}\cdot A$ cluster intensity as well as the average number of photons i.e. $[Int_{FRAG}/Int_{OFF}]/(\lambda \cdot P)$, where Int_{FRAG} is the intensity of fragment ions produced following photodissociation [26].

Electron detachment (ED) yield spectra were calculated by assuming that any depleted ions not detected as ionic photofragments are decaying by electron detachment, i.e. the electron detachment yield = [(photodepletion ion count – Σ photofragment ion counts)/Int_{OFF}]/(λ·P). This analysis assumes that both the parent ions and photofragments are detected equally in the mass spectrometer, a reasonable assumption for the systems studied here where the parent ions and fragment ions are reasonably close in m/z. In the figure where we present ED spectra (Figure 7), we overlay this data with the photodepletion yield (PD*). PD* is the normalized photodepletion ion count, i.e. PD*= $[(Int_{OFF}-Int_{ON})/Int_{OFF})]/(\lambda \cdot P)$, which provides the most straightforward comparison to the electron detachment yield [27].

The geometric structures of the $X^{-}\cdot A$ clusters were studied computationally with Gaussian 09 [28]. Cluster structures of the X^{-} ions coordinated to known adenine isomers were optimised at the B3LYP/6-311++G(2d,2p) level of theory on C, N, O, and H, and 6-311G(d,p) on I, with the iodine core electrons being described using the Stuttgart/Dresden (SDD) electron core pseudopotential. MP2 and M06-2X level calculations were performed to calculate the dipole moments and the spin densities, respectively. Cluster binding energies were calculated using the counterpoise correction method. Frequency calculations were performed after all geometry optimisations to ensure that the optimised structures correspond to true energy minima. To

calculate the electronic excitations, time-dependent density functional theory (TD-DFT) calculations (50 states) were performed on the lowest-energy X^-·A optimised isomers.

3. Results

3.1 Geometric Structures of X^-·A Clusters

(Figure 2)

Figure 2 shows the two lowest-energy calculated structures of the X^-·A (X^-=I^- and $H_2PO_3^-$) clusters, with Table 1 listing the corresponding relative energies and other properties. In the $H_2PO_3^-$·A structures, the dihydrogen phosphite anion forms a bifurcated hydrogen bond across NH and CH groups. Similar structures have been observed using IR spectroscopy for NO_3^- and HCO_3^- in their clusters with water [29]. For the I^-·A structures, the iodide ion is again involved in two hydrogen bonds to adenine, although in the I^-·A9 structure, one of these hydrogen bonds is close to a typical linear geometry.

In the $H_2PO_3^-$·A7 complex, the iodide ion is bound along the axis of the permanent electric dipole moment of A7. It is notable that the A7 dipole moment is higher than that of A9 so that in these dominantly ion-dipole complexes [20], the A7 tautomer is present in the lowest-energy cluster, with the biologically active tautomer cluster, A9, being found at relatively higher energy. The binding energies of both X^-·A7 clusters are significantly higher than those of the X^-·A9 clusters, again consistent with their ion-dipole nature. From the calculated room-temperature Boltzman population at room temperature (Table 1), we expect the A7 isomer clusters to be dominant in our electrosprayed ions. The A9 isomer will not be visible in the experimental spectra, as it is expected to be four orders of magnitude less populated that the A7 isomer cluster.

(Table 1)

Neumark and co-workers have measured the VDE values of the $I^-\cdot A9$ and $I^-\cdot A3$ clusters previously, and our calculated VDEs are in good agreement with these previous results [19]. Although they were also working in the gas-phase, their experiment uses an electron gun-molecular beam set-up to produce clusters, an approach that does not produce the $I^-\cdot A7$ isomer.

The VDE values calculated here warrant further comment. For the iodide ion clusters, the calculated VDE is in line with a value for an anionic ion-dipole complex, which transfers to a neutral complex where the iodine atom interacts only very weakly with the adenine once the electron is removed. In such systems, the VDE of the cluster is effectively blue-shifted from the electron binding energy of the bare iodide ion by the cluster ion-molecule binding energy (~1 eV) [30, 31]. However, this is not the case for the $H_2PO_3^-$ cluster. We calculate that bare $H_2PO_3^-$ has a VDE of 4.73eV, so that the calculated VDE of the $H_2PO_3^-\cdot A$ complexes is considerably lower than would be expected if a weakly-interacting neutral cluster results once the electron is removed. Wang and Kass have observed similar 'reduced electron binding energy' in hydrogen-bonded anion clusters previously [32].

TD-DFT spectra of the lowest-energy $X^-\cdot A7$ clusters have also been calculated and are shown in Figure 3. As we have discussed previously [27], such calculations are not expected to accurately predict dipole-bound excited states, since tailored, diffuse functionals are necessary to accurately mimic dipole-bound orbitals [33-35]. The TD-DFT calculations predict a strong transition around 4.8 eV for both $X^-\cdot A7$ clusters, which is associated with a nucleobase-localized $\pi \rightarrow \pi^*$ excitation. The two spectra differ mainly in the number and the intensity of the predicted charge-transfer transitions, which arise from the n orbital on X^-. Intriguingly, these are far more numerous for the $I^-\cdot A7$ cluster. We note that similar charge-transfer

transitions have recently been calculated by Mensa-Bonsu et al. to appear in the near-threshold region of the $I^-\cdot CF_3I$ complex [36].

(Figure 3)

3.2 Photodepletion of the $X^-\cdot A$ Clusters

Photodepletion spectra of the $X^-\cdot A$ clusters across the range 3.8-5.8 eV are shown in Figure 4. These spectra correspond to gas-phase absorption spectra in the limit where the excited states decay without fluorescence [37]. However, it is important to note that at energies above the VDEs, the spectra will reflect contributions from electron detachment, as well as intra-cluster electronic excitations.

Figure 4a displays the photodepletion spectrum for $I^-\cdot A$, with a photodepletion onset at ~4.0 eV and two bands (**I** and **II**) with λ_{max} at ~ 4.4 and ~ 5.2 eV, respectively. Above band **I**, the absorption cross section is relatively flat before rising again towards the band **II** maximum, with a distinct shoulder visible below band **I** at ~ 4.2 eV. Comparison of the spectral profile of the $I^-\cdot A$ spectrum to those of similar clusters we have studied previously [30, 38], suggests that the VDE of the $I^-\cdot A$ cluster present in our experiment is ~ 4.2 eV. Our calculated VDE for $I^-\cdot A7$ is included on the spectrum shown in Fig. 4a.

The photodepletion spectrum of $H_2PO_3^-\cdot A$ is shown in Figure 4b, with an onset above ~4.3 eV leading up to a broad band with a maximum at 4.7 eV (labelled **I**). A shoulder is again visible below band **I** at ~4.4 eV. In contrast to $I^-\cdot A$, the $H_2PO_3^-\cdot A$ spectrum decreases after band **I** until around 5.4 eV when it starts increasing strongly to the high-energy spectral edge. The calculated VDE for $H_2PO_3^-\cdot A7$ is again included on the spectrum shown in Figure 4b.

(Figure 4)

3.3 Photofragmentation of the $X^{-}\cdot A$ Clusters

To further explore the nature of the excited states that are evident in the photodepletion spectra (Figure 4), the photofragment production spectra of the $X^{-}\cdot A$ clusters were investigated. Each cluster was found to produce both $[A\text{-}H]^{-}$ and X^{-} as photofragment ions. For $I^{-}\cdot A$, the $[A\text{-}H]^{-}$ photofragment was produced approximately ten times more strongly than the I^{-} photofragment, while for $H_2PO_3^{-}\cdot A$, both photofragments were produced with similar intensities.

(Figure 5)

The photofragment action spectra obtained from excitation of $I^{-}\cdot A$ are shown in Figure 5, and reveal that the $[A\text{-}H]^{-}$ and I^{-} photofragments display dramatically different production spectra. The more intense photofragment $[A\text{-}H]^{-}$ is produced very strongly over the lower-energy spectral region, peaking at ~ 4.2 eV within band **I** (Figure 4a). We note that this energy is very close to the VDE calculated for $I^{-}\cdot A7$ (4.34 eV). A slight increase in $[A\text{-}H]^{-}$ production is also evident in the region leading up to 5.2 eV (~2% the intensity of band **I**). For the I^{-} photofragment, the product spectrum has an onset at ~ 4.0 eV, with a small maximum at ~ 4.2 eV (close to the maximum in $[A\text{-}H]^{-}$ production) and a flat profile with a small intensity enhancement at ~ 5.1 eV.

Figure 6 displays the photofragment action spectra of the primary $H_2PO_3^{-}\cdot A$ photofragments, $H_2PO_3^{-}$ and $[A\text{-}H]^{-}$ (this cluster also produces PO_3^{-} as a very minor photofragment, the relevant spectrum is included in section S3 of the SM). The production spectra of the $H_2PO_3^{-}$ and $[A\text{-}H]^{-}$ photofragments are again different from one another, with neither of these production spectra being similar to the photofragment spectra observed for $I^{-}\cdot A$ (Figure 5). The $[A\text{-}H]^{-}$ photofragment (Figure 6a) is produced across the whole region from 4.3 to 5.4 eV, with the photofragment intensity decreasing to the high-energy spectral edge. For the $H_2PO_3^{-}$

photofragment (Figure 6b), the production spectrum is also very broad, peaking between 4.8-5.2 eV. Above 5.2 eV, $H_2PO_3^-$ production decreases up to ~ 5.6 eV, but then starts increasing again.

(Figure 6)

The distinctive photofragment profiles from $I^-\cdot A$ and $H_2PO_3^-\cdot A$ reveal that the decay pathways following photoexcitation are different for the two clusters. However, in both cases, it is notable that all of the photofragments are produced with very small intensities, so that electron detachment represents the main photodepletion channel. This is discussed further in Section 3.4.

3.4 Electron Detachment Yield Spectra of the $X^-\cdot A$ Clusters

Figure 7 shows the electron detachment yields for the $X^-\cdot A$ clusters overlaid with the photodepletion yield (PD*) for comparison. It is notable that, for both $X^-\cdot A$ clusters, the electron detachment and the modified photodepletion spectra largely overlap, except where ionic photofragmentation is maximised between 4.1-4.4 eV for $I^-\cdot A$ (Figure 7a) and 4.8 to 5.4 eV $H_2PO_3^-\cdot A$ (Figure 7b). Even in these regions, however, the difference between electron detachment and photodepletion is small, indicating a high yield of electron detachment.

(Figure 7)

4. Discussion

4.1 Overview on Decay Channels

Before discussing the results in more detail, it is useful to consider the possible decay pathways for the $X^-\cdot A$ clusters. The first group of cluster decay channels result in fragmentation:

$$X^-\cdot A + h\nu \rightarrow X + A^- \quad (1a)$$

$$\rightarrow X^- + A \quad (1b)$$

$$\rightarrow \quad HX + [A\text{-}H]^- \qquad (1c)$$

Alternatively, electron detachment can occur above the electron detachment threshold, either *via* direct detachment (2a) or indirectly from an excited state of the cluster (2b). Electron detachment can also occur from hot photofragments, e. g. (2c) and (2d).

$$X^-\cdot A \rightarrow X\cdot A + e^- \qquad (2a)$$

$$\rightarrow [X\cdot A]^{*-} \rightarrow [X\cdot A] + e^- \qquad (2b)$$

$$\rightarrow HX + [A\text{-}H]^{*-} \rightarrow HX + [A\text{-}H] + e^- \qquad (2c)$$

$$\rightarrow X + A^{*-} \rightarrow X + A + e^-. \qquad (2d)$$

The ionic fragmentation products observed following photoexcitation of the $X^-\cdot A$ clusters are produced with very low intensities (Section 3.2), in line with pathways (2a)-(2d) dominating the cluster decay.

An additional possibility has been suggested by Wang and Kass, where electron detachment leads to the transfer of hydrogen, either as a hydrogen atom or as a proton, on the neutral surface. For the $X^-\cdot A$ clusters studied here,

Hydrogen atom transfer: $X^-\cdot A + h\nu \rightarrow e^- + X\cdot A \rightarrow XH\cdot [A\text{-}H]$ [3a]

Proton transfer: $X^-\cdot A + h\nu \rightarrow e^- + [X^-\cdot A^+] \rightarrow XH\cdot [A\text{-}H]$ [3b]

4.2 Assignment of the Excited States of the $X^-\cdot A$ Clusters

Band **I** in the photodepletion spectrum of $I^-\cdot A$ (Figure 4a) peaks at 4.4 eV with a partially-resolved shoulder evident at 4.17 eV. The VDE of the $I^-\cdot A9$ form of the cluster was measured as 3.96 eV by Neumark and co-workers [19], and they also observed a dipole-bound (DB) state for this tautomer slightly below the VDE. The absence of any depletion of $I^-\cdot A$ below 4 eV in this work indicates that the $I^-\cdot A9$ tautomer is not present in the electrospray generated ion ensemble in our experiment, as predicted by our calculated relative energies (Table 1). Indeed, our calculations indicate that the dominant cluster tautomer that should be present in our

experiment is I^-·A7, which is predicted to have a VDE of 4.34 eV. This calculated value is close to the band **I** maximum, strongly indicating that a dipole-bound excited state of I^-·A7 is being accessed in this region. We have previously shown that dipole-bound excited states can be observed in our instrument following near-threshold anion excitation [27, 38, 39]. The identity of the shoulder peak at 4.17 eV resembles similar structures present in the near-threshold photodepletion spectra of anionic alkali halide clusters (e.g. I^-·NaI) [38], which were assigned to excitation of the vibrational envelope in the dipole-bound excited state of the cluster.

At higher energies, an enhancement on the flat photodepletion region is evident at ~5.2 eV, labelled **II** on Figure 4a. This photodepletion enhancement is also evident in the I^- action spectrum (Figure 5b). Indeed, if we focus on the I^- action spectrum, band **I** appears clearly at ~4.2 eV with band **II** at ~5.2 eV, leading us to assign these features to the two spin-orbit states of the neutral cluster ($^2P_{1/2}$ and $^2P_{3/2}$, respectively), which are separated by 0.94 eV for iodine [16,30]. Band **II** in the photofragmentation spectrum is therefore assigned as arising from direct detachment from the dipole-bound excited state built on the upper ($^2P_{1/2}$) spin-orbit state of I [18, 40].

The TD-DFT calculations for I^-·A7 predict a $\pi \rightarrow \pi^*$ transition at 4.9 eV, centred on the adenine moiety, with numerous charge-transfer transitions occurring across the spectral range. No distinct band around this energy is visible in either the photodepletion spectrum of I^-·A7 or its photofragmentation action spectra, presumably due to the relative strength of electron detachment. Some of the calculated $\pi \rightarrow \pi^*$ transitions are coupled to $n \rightarrow \sigma^*$ transitions (at 4.86 and 4.90 eV), reflecting similar results to the related I^-·C [32].

For $H_2PO_3^-\cdot A$, the photodepletion spectrum again displays an onset in the region close to the calculated VDE of the cluster. The strong absorption close to 4.8 eV corresponds to the well-known $\pi \rightarrow \pi^*$ transition on adenine moiety [41], which appears prominently in the TD-DFT calculated spectrum. Above 5.4 eV, photodepletion and production of $[H_2PO_3]^-$ begin to increase strongly, correlating with excitation of the $\pi \rightarrow \sigma^*$ transition (5.65 eV) predicted by the TD-DFT calculation in this region (see section S2 of SM).

4.3 Photofragment Production

The production of ionic photofragments from anions clustering with neutral neucleobase is usually explained *via* two main mechanisms [15]: an electron transfer from the anion (either through the formation of a dipole-bound excited state, followed by the emission of a low-energy electron that interacts with the nucleobase, or a direct electron transfer to a valence orbital of the nucleobase) or from a transition localized on the nucleobase moiety.

From the first-type of process, we expect the production of the adenine, A^- (1a), or the deprotonated adenine anion $[A\text{-}H]^-$ (1c). In contrast, the adenine-centred transitions within the cluster are expected to produce the cluster fragments that are associated with thermal fragmentation of the ground-electronic state [25], following ultrafast decay of the initially populated nucleobase-localized electronic excited state.

To identify the fragments that are produced upon thermal dissociation of the cluster ground electronic states, higher-energy collisional dissociation (HCD) of the $X^-\cdot A$ clusters was performed (see Section S1 of the SM for further details) [41]. HCD over a wide collisional energy range revealed that $I^-\cdot A$ produces I^- as the only ionic fragment, whilst $H_2PO_3^-\cdot A$ produces both $H_2PO_3^-$ and $[A\text{-}H]^-$. The HCD profiles of these fragments are distinctive, with the $H_2PO_3^-$ being produced with a steeper onset from 0-12 %, but with a decreasing intensity above 20 %, while the $[A\text{-}H]^-$ fragment production profile increasing only modestly across the collisional

range from 4-45 %. It is notable that the relative intensity of $[A\text{-}H]^-$ compared to $H_2PO_3^-$ is greater in the photodissociation experiment than in HCD.

The production of the $[A\text{-}H]^-$ photofragment from $I^-\cdot A$ in the region of the VDE, is consistent with excitation of a dipole-bound excited state, that facilitates capture of the excess electron into the valence orbitals of adenine, with subsequent ejection of a hydrogen atom and $[A\text{-}H]^-$. The production channel for $[A\text{-}H]^-$ drops very sharply at energies above the VDE due to autodetachment from the valence anion at higher internal energies. Ref [17, 30]. Production of I^- would be expected in the region of the adenine localised π-π^* transition, but instead it is observed weakly across the whole above-threshold region. This is a phenomenon that we have observed previously, since $I^-\cdot U$ also produced an I^- photofragment across a wide excitation range [15]. We attributed this behaviour to internal conversion to the ground electronic state followed by evaporation of I^-, possibly mediated by the weak charge transfer excitations that were predicted to occur across the spectral range. The behaviour of $I^-\cdot A$ seen here appears very similar, with the caveat that the $[A\text{-}H]^-$ fragment is produced relatively more strongly across the region close to the VDE. This indicates that the dissociative electron attachment cross section is significantly greater for adenine than for the other nucleobases within these clusters, i.e. within the neutral $I\cdot A$ cluster which is formed upon electron detachment. (We note that little attention has been paid in electron attachment experiments to the nature of the nucleobase tautomers present [42, 43], and this may mean that results for the isolated nucleobases are not directly comparable to the clusters studied here).

For $H_2PO_3^-\cdot A$ (Figure 6a), all the thermal ground state fragments (see S1 and S3 of SM for detail) are produced as photofragments following cluster excitation across the entire spectral range. By comparison to $I^-\cdot A$ and also $I^-\cdot U$, this suggests that the excited states of the $H_2PO_3^-$

·A cluster are able to ultimately decay across a wide spectral range via internal conversion to a hot ground state. It is notable that the shape of the photofragment production profiles (Figure 6) mirrors the production profiles of the corresponding HCD fragments (Section S1), with $H_2PO_3^-$ being produced relatively more strongly at the lower and higher collision energies than $[A\text{-}H]^-$. This similarity between the HCD fragment profiles and photofragment production profiles is indicative of cluster relaxation via ultrafast internal relaxation and ground state thermal fragmentation. Ionic fragmentation of $H_2PO_3^-$·A is therefore largely associated with relaxation of electronic excitations localized on the adenine moiety.

Finally, it is useful to reflect on the relationship between photofragmentation and electron detachment that is revealed by the spectra presented in Figure 7. For I^-·A, the biggest difference between photodepletion and electron detachment (i.e. the region where the most ionic fragments are produced) occurs close to the VDE, characteristic of the presence of a dipole-bound state, whereas for $H_2PO_3^-$·A, the region where the most ionic photofragments are produced occurs through a region centred at 5.2 eV, close to where the adenine-localized $\pi \rightarrow \pi^*$ transition is predicted to occur by the TD-DFT calculations.

5. Further Discussion

Comparing the photophysics of the I^-·A cluster with our recent results on I^-·pyrimidine clusters [27], two main differences are apparent. Firstly, the relative abundances of the two characteristic photofragments produced by these clusters (i.e. I^- and $[M\text{-}H]^-$), with $[A\text{-}H]^-$ being the dominant fragment for the I^-·A cluster in contrast to the I^-·pyrimidine clusters where the I^- photofragment is more intense. This phenomenon reflects the relative dissociative electron attachment properties of adenine versus uracil within the two clusters, i.e. in I.A versus I.U.

Secondly, in $I^-\cdot A$, no significant enhancement in $[A-H]^-$ production is observed in the region of the adenine $\pi \rightarrow \pi^*$ transition, in contrast to $I^-\cdot U$ and $I^-\cdot T$. $I^-\cdot A$ mirrors the behaviour of $I^-\cdot C$, where it was attributed to a relatively weaker $\pi \rightarrow \pi^*$ transition around 4.8 eV for cytosine compared to uracil and thymine.[27]

The photodepletion spectrum of $H_2PO_3^-\cdot A$ closely resembles those of gaseous deprotonated ATP, ADP and AMP anions [41]. In the photodissociation study of this series of related bioanions anions, it was concluded that the adenine photochemistry was independent of the excess charge of the system or the length of the phosphate chain present. In a related series of experiments on the 3′-deoxy-adenosine-5′monophosphate nucleotide, and its di and trinucleotides, Verlet and co-workers showed that the adenine dynamics are similarly insensitive to the surrounding environment, with excitation of the prominent $\pi \rightarrow \pi^*$ state and subsequent relaxation back to the ground state dominating the photodynamics [44]. It is very notable that the photofragment production profile that we observe for $[A-H]^-$ in the region between 4.4 and 5.4 eV closely resembles the one observed following photoexcitation of $[ADP-H]^-$ (including the small sub-peak in $[A-H]^-$ production in the region between 4.4 and 4.6 eV close to the VDE). This strongly suggests that the chromophores and excited state morphology is similar in the two systems, and dominated by the adenine moiety.

There are two possible explanations for the differences in the photophysics of the anion-adenine clusters observed here, linked to the fact that a near-threshold dipole-bound excited state dominates the photophysics of the $I^-\cdot A$ cluster, while such a state appears entirely absent for $H_2PO_3^-\cdot A$. At the simplest level, the absence of a dipole-bound excited state for $H_2PO_3^-\cdot A$ could be traced to the nature of the anion-centred excess electron density of $H_2PO_3^-\cdot A$ compared to that in $I^-\cdot A$. The more delocalized electronic density on $H_2PO_3^-\cdot A$ will have a poorer Franck

Condon overlap with a potential dipole-bound excited state thus reducing the transition intensity. However, if this were the only effect, we might still expect to see a relatively weak dipole-bound state in the region of the electron detachment energy for $H_2PO_3^-\cdot A$.

It is more convincing that the difference in photophysics displayed by $I^-\cdot A$ and $H_2PO_3^-\cdot A$ is linked to the reduced electron binding energy of $H_2PO_3^-\cdot A$ noted in Section 3.1. This lower electron binding energy is associated with hydrogen motion within the complex after electron detachment (Equations 3a and 3b). In this case, electron detachment leads to significant geometric rearrangement on the neutral surface, which ultimately produces the neutral [A-H] moiety, possibly within an intact $H_3PO_4\cdot$[A-H] complex. Such a system clearly cannot be described as equivalent to $I^-\cdot A$ where the iodine is described as a spectator atom upon electron detachment [11]. Wang and Kass have explained the phenomena of hydrogen atom/proton transfer on the neutral surface as arising from a lowering of the ionization energy of the neutral moiety in the initial cluster [32]. Evidence for this can be found by considering the spin densities of the detached complexes, as if the ionization energy of the neutral is reduced, it may be ionized rather than the anion.

Figure 8 presents spin density plots for $I^-\cdot A$ and $H_2PO_3^-\cdot A$. The difference is striking, as the calculations reveal that the excess electron is removed from the iodine in $I^-\cdot A$ but from the adenine moiety in $H_2PO_3^-\cdot A$. These calculations support the idea that $H_2PO_3^-\cdot A$ is a system where significant geometric rearrangement occurs on the neutral surface. Indeed, these spin-density calculations indicate that the $I^-\cdot A$ and $H_2PO_3^-\cdot A$ clusters represent two extreme limits of behaviour with respect to electron ejection. Of key importance is the fact that the geometric rearrangement on the neutral surface for detached $H_2PO_3^-\cdot A$ will mean that there is significant difference between the adiabatic electron affinity and the vertical detachment energy for the

system. This will lead to negligible Franck-Condon overlap between the anionic ground state complex and any dipole-bound excited state.

(Figure 8)

Summarising, it is clear that $H_2PO_3^-\cdot A$ does not represent a system where the anion can be considered a spectator to allow the study of molecular electron capture within a cluster, and this study clearly demonstrates the importance of carefully selecting the anionic charge carrier for studies where a 'spectator' electron source is required. $H_2PO_3^-\cdot A$ evidently provides a new example of a novel anionic cluster system where ionization occurs from the neutral component of the cluster, and where photoinduced hydrogen atom/proton electron transfer occurs. The system therefore represents a key example as a target for future time-resolved measurements.

Acknowledgements

We thank the University of York and the Department of Chemistry for provision of funds for the Horizon OPO laser system and the York Advanced Computing Cluster (YARCC) for access to computational resources. R.C. thanks the Department of Chemistry at the University of York for funding *via* a departmental studentship. We also acknowledge the facilities of the York Centre of Excellence in Mass Spectrometry, which was created thanks to a major capital investment through Science City York, supported by Yorkshire Forward with funds from the Northern Way Initiative, and subsequently received additional support from the EPSRC.

References

[1] B. Boudaiffa, P. Cloutier, D. Hunting, M.A. Huels and L. Sanche, Science **287**, 1658 (2000).

[2] L. Sanche, Eur. Phys. J. D **35**, 367 (2005).

[3] J.K. Wolken and F. Turecek, J. Phys. Chem. A **105**, 8352 (2001).

[4] S.G. Ray, S.S. Daube and R. Naaman, Proc. Natl. Acad. Sci. U.S.A. **102**, 15 (2005).

[5] H. Abdoul-Carime, S. Gohlke and E. Illenberger, Phys. Rev. Lett. **92**, 168103 (2004).

[6] I. Baccarelli, I. Bald, F.A. Gianturco, E. Illenberger and J. Kopyra, Phys. Rep. **508**, 1 (2011).

[7] H. Abdoul-Carime, S. Gohlke, E. Fischbach, J. Scheike and E. Illenberger, Chem. Phys. Lett. **387**, 267 (2004).

[8] J.D. Gu, J. Leszczynski and H.F. Schaefer, Chem. Rev. **112**, 5603 (2012).

[9] S.M. Pimblott and J.A. LaVerne, Radiat. Phys. Chem. **76**, 1244 (2007).

[10] L.Sanche, Radiat. Phys. Chem. **34**, 15 (1989).

[11] M.A. Yandell, S.B. King and D.M. Neumark, J. Am. Chem. Soc. **135**, 2128 (2013).

[12] S.B. King, M.A. Yandell, and D.M. Neumark, Faraday Disscus. **163**, 59 (2013).

[13] S.B. King, M.A. Yandell, A.B. Stephansen and D.M. Neumark, J. Chem. Phys. **141**, 224310 (2014).

[14] S.B. King, A.B. Stephansen, Y. Yokoi, M.A. Yandell, A. Kunin, T. Takayanagi and D.M. Neumark, J. Chem. Phys. **143**, 024313 (2015).

[15] W.L. Li, A. Kunin, E. Matthews, N. Yoshikawa, C.E.H. Dessent and D.M. Neumark, J. Chem. Phys. **145**, 044319 (2016).

[16] C.E H. Dessent, C.G. Bailey and M.A. Johnson, J. Chem. Phys. **105**, 10416 (1996).

[17] C.E.H. Dessent, J. Kim and M.A. Johnson, Faraday Discuss. **115**, 395 (2000).

[18] F. Mbaiwa, M. Van Duzor, J. Wei and R. Mabbs, J. Phys. Chem. A **114**, 1539 (2010).

[19] A.B. Stephansen, S.B. King, Y. Yokoi, Y. Minoshima, W.L. Li, A. Kunin, T. Takayanagi and D.M. Neumark, J. Chem. Phys. **143**, 104308 (2015).

[20] M. Schreiber and L. Gonzalez, J. Comput. Chem. **28**, 2299 (2007).

[21] C. Desfrancois, H. Abdoul-Carime and J.P. Schermann, J. Chem. Phys. **104**, 7792, (1996).

[22] M. Haranczyk, M. Gutowski, X. Li and K.H. Bowen, Proc. Natl. Acad. Sci. U.S.A. **104**, 4804 (2007).

[23] E.D. Raczynska, M. Makowski, K. Zientara-Rytter, K. Kolczynska, T.M. Stepniewski, and M. Hallmann, J. Phys. Chem. A **117**, 1548 (2013).

[24] E. Matthews, A. Sen, N. Yoshikawa, E. Bergstrom and C.E.H. Dessent, Phys. Chem. Chem. Phys. **18**, 15143 (2016).

[25] A. Sen, T.F.M. Luxford, N. Yoshikawa and C.E.H. Dessent, Phys. Chem. Chem. Phys. **16**, 15490 (2014).

[26] I. Compagnon, A.R. Allouche, F. Bertorelle, R. Antoine and P. Dugourd, Phys. Chem. Chem. Phys. **12**, 3399 (2010).

[27] E. Matthews, R. Cercola, G. Mensa-Bonsu, D.M. Neumark and C.E.H. Dessent, J. Chem. Phys. **148**, 084304 (2018).

[28] M.J. Frisch, G.W. Trucks, H.B. Schlegel, G.E. Scuseria, M.A. Robb, J.R. Cheeseman, G. Scalmani, V. Barone, B. Mennucci, G.A. Petersson, H. Nakatsuji, M. Caricato, X. Li, H.P. Hratchian, A.F. Izmaylov, J. Bloino, G. Zheng, J.L. Sonnenberg, M. Hada, M. Ehara, K. Toyota, R. Fukuda, J. Hasegawa, M. Ishida, T. Nakajima, Y. Honda, O. Kitao, H. Nakai, T. Vreven, J.J.A. Montgomery, J.E. Peralta, F. Ogliaro, M. Bearpark, J.J. Heyd, E. Brothers, K.N. Kudin, V.N. Staroverov, R. Kobayashi, J. Normand, K. Raghavachari, A. Rendell, J.C. Burant, S.S. Iyengar, J. Tomasi, M. Cossi, N. Rega, J.M. Millam, M. Klene, J.E. Knox, J.B. Cross, V. Bakken, C. Adamo, J. Jaramillo, R. Gomperts, R.E. Stratmann, O. Yazyev, A.J. Austin, R. Cammi, C. Pomelli, J.W. Ochterski, R.L. Martin, K. Morokuma, V.G. Zakrzewski, G.A. Voth, P. Salvador, J.J. Dannenberg, S. Dapprich, A.D. Daniels, O. Farkas, J.B. Foresman, J.V. Ortiz, J. Cioslowski and D.J. Fox, Gaussian 09, Revision D.01 (Gaussian, Wallingford, CT, 2009).

[29] K.R. Asmis and D.M. Neumark, Acc. Chem. Res. **45**, 52 (2012).

[31] C.E.H. Dessent, C. G. Bailey and M. A. Johnson, J. Chem. Phys. **103**, 2006 (1995).

[31] A.W. Castleman Jr. and K.H. Bowen Jr., J. Phys. Chem. **100**, 12911 (1996).

[32] X.B. Wang and S.R. Kass, J. Am. Chem. Soc. **136**, 17332 (2014).

[33] M. Gutowski and P. Skurski, J. Phys. Chem. A **102**, 2624 (1998).

[34] P. Skurski, M. Gutowski and J. Simons, Int. J. Quantum Chem. **80**, 1024 (2000).

[35] W.J. Morgan and R.C. Fortenberry, Theor. Chem. Acc. **134**, 47 (2015).

[36] G. Mensa-Bonsu, D.J. Tozer and J.R.R. Verlet**,** Phys. Chem. Chem. Phys. Advance Article (2019).

[37] S.M.J. Wellman and R.A. Jockusch, J. Phys. Chem. A **119**, 6333 (2015) .

[38] A.J.A. Harvey, N. Yoshikawa, J.G. Wang, and C.E.H. Dessent, J. Chem. Phys. **143**, 101103 (2015).

[39] E. Matthews and C.E.H. Dessent, J. Phys. Chem. Lett. **9**, 6124, (2018).

[40] F. Mbaiwa, D. Dao, N. Holtgrewe, J. Lasinski, and R. Mabbs, J. Chem. Phys. **136**, 114303 (2012).

[41] R. Cercola, E. Matthews and C.E.H. Dessent, J. Phys. Chem. B **121**, 5553 (2017).

[42] K. Aflatooni, A. M. Scheer and P.D. Burrow, J. Chem. Phys. **125**, 054301 (2006)

[43] S. Denifl, S. Ptasińska, G. Hanel, B. Gstir, M. Probst, P. Scheier and T.D. Märk, J. Chem. Phys. **120**, 6557 (2004)

[44] A.S. Chatterley, C.W. West, G.M. Roberts, V.G. Stavros and J.R.R. Verlet, J. Phys. Chem. Lett. **5**, 843 (2014).

Table 1. Properties of the $X^{-}\cdot A$ clusters calculated at the B3LYP/6-311++G(2d,2p) theory level, with 6-311G(d,p)/SDD for I^{-}.

Cluster	**Relative Energy** kJ mol^{-1}	**Boltzman population**[a] %	**VDE Calc.** eV	**Exp. VDE**[b] eV	**Binding Energy** kJ mol^{-1}
$I^{-}\cdot A7$	0.0	100	4.34		134
$I^{-}\cdot A9$	20.8	$2.27x10^{-2}$	4.08	3.96	82.3
$I^{-}\cdot A3$	42.1	$4.21x10^{-6}$	4.13	4.11	63
$H_2PO_3^{-}\cdot A7$	0.0	100	4.66		177
$H_2PO_3^{-}\cdot A9$	25.6	$3.27x10^{-3}$	4.92		118
$H_2PO_3^{-}\cdot A3$	44.4	$1.66x10^{-6}$	4.90		134

a) Room temperature.

b) Ref. 19.

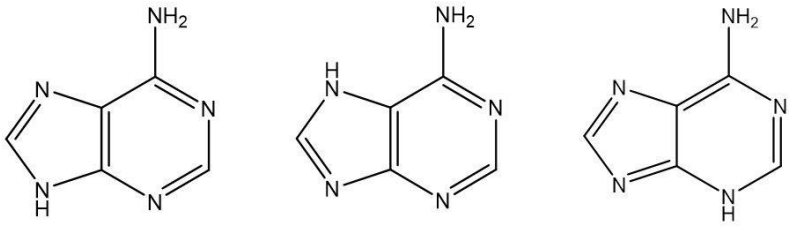

Figure 1

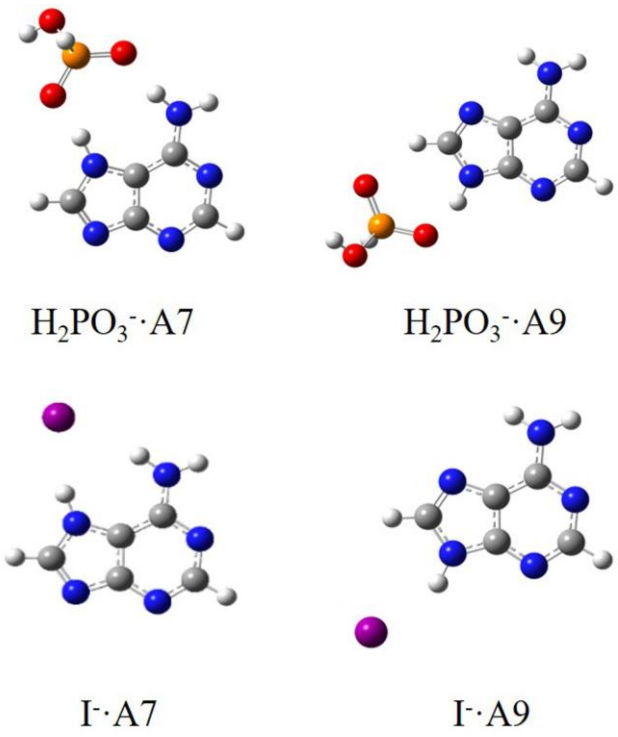

Figure 2

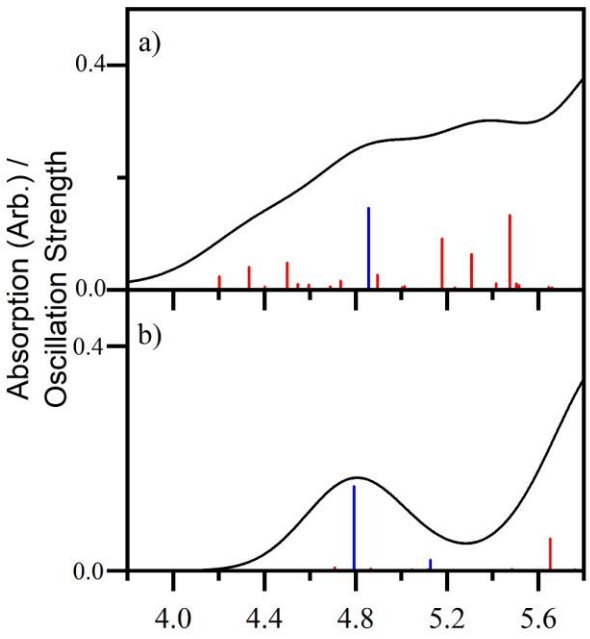

Figure 3

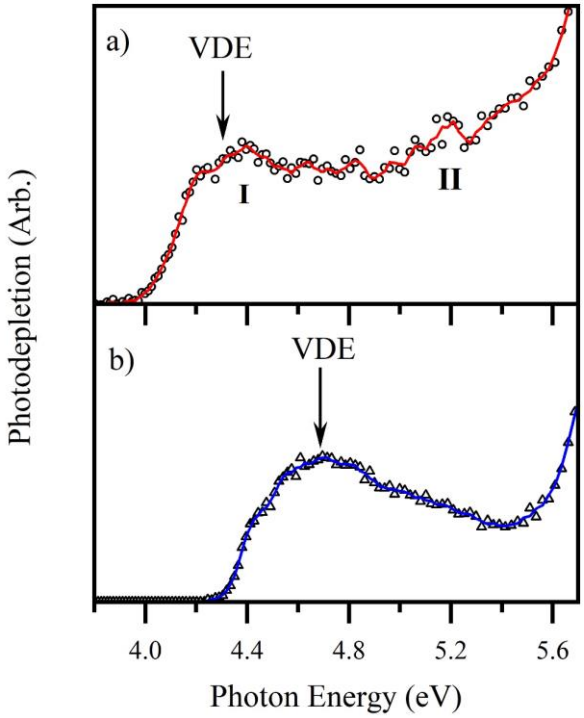

Figure 4

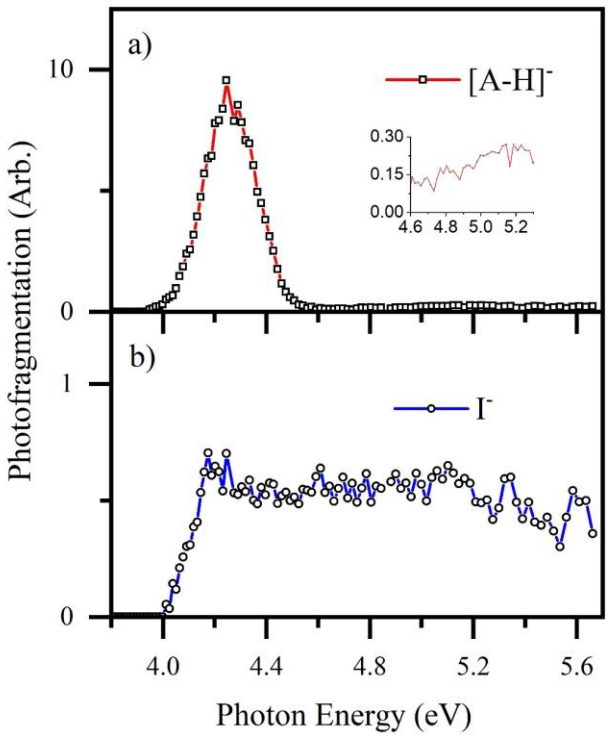

Figure 5

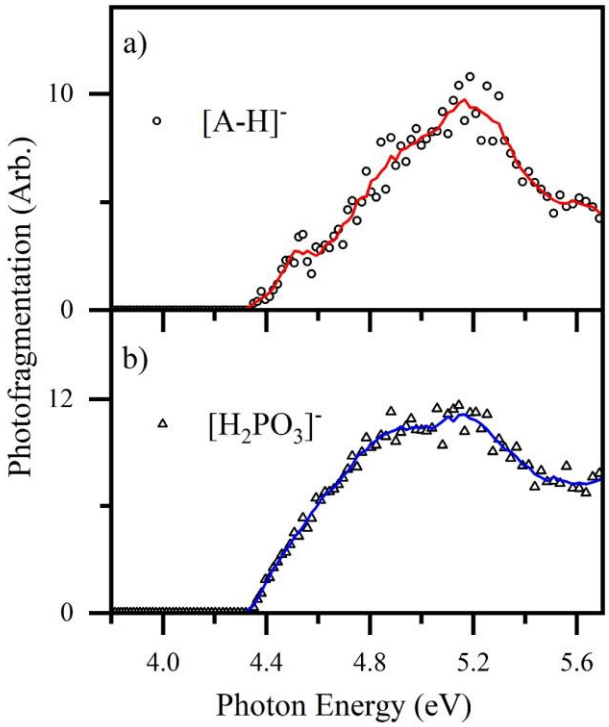

Figure 6

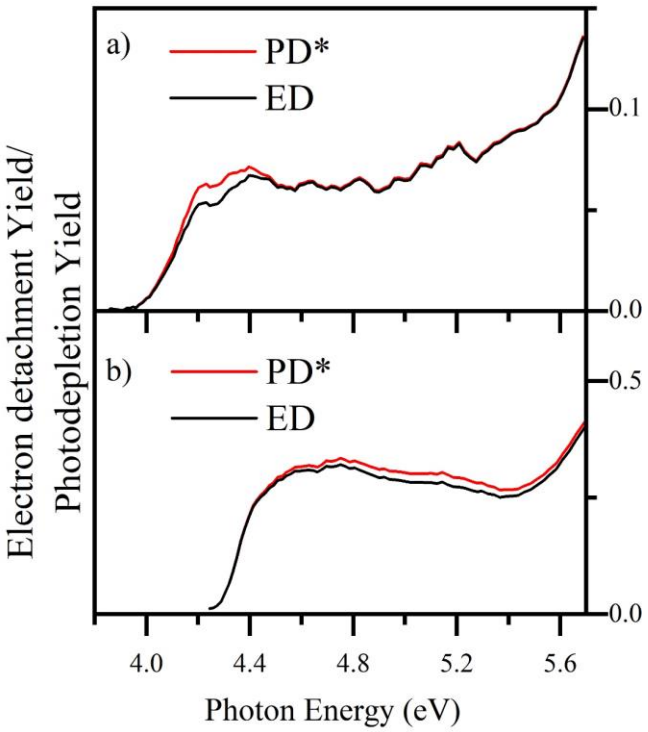

Figure 7

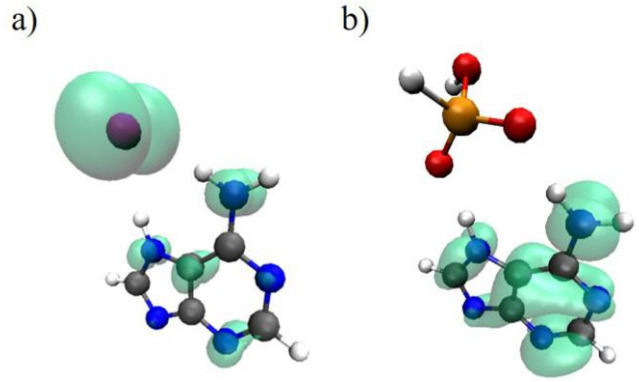

Figure 8

Figure 1. Structures of the A9, A7 and A3 amine tautomers of adenine. Top left: adenine amine-9H (A9), centre: adenine amine-7H (A7) and top right: adenine amine-3H (A3). Calculated dipole moments of the tautomers are also shown [20].

Figure 2. The lowest-energy calculated structures of the $X^{-}\cdot A$ clusters. See text for details.

Figure 3. TD-DFT calculated spectra (50 states) of (a) $I^{-}\cdot A7$ and (b) $H_2PO_3^{-}\cdot A7$. The oscillator strengths of the strongest transitions are given by the vertical bars. Blue lines are $\pi \rightarrow \pi^*$ transitions. The full black line spectrum represents a convolution of the calculated spectrum with a Gaussian function (0.25 eV HWHM).

Figure 4. Photodepletion spectra of (a) $I^{-}\cdot A$ and (b) $H_2PO_3^{-}\cdot A$. The lines are five-point adjacent average of the data points. Calculated VDEs for $I^{-}\cdot A7$ and $H_2PO_3^{-}\cdot A7$ are shown on the spectra.

Figure 5. (a) $[A-H]^{-}$ and (b) I^{-} photofragment action spectra produced from the $I^{-}\cdot A$ cluster. The insert in (a) shows the expanded action spectrum of $[A-H]^{-}$ between 4.6 and 5.3 eV.

Figure 6. (a) $[A-H]^{-}$ and (b) $H_2PO_3^{-}$ photofragment action spectra produced from the $H_2PO_3^{-}\cdot A$ cluster. The lines are five-point adjacent average of the data points.

Figure 7. Photodepletion yield (PD*) and electron detachment yield (ED) of the $I^{-}\cdot A$ (a) and $H_2PO_3^{-}\cdot A$ (b) clusters. The curves are five-points adjacent averages of the data points. PD* and ED are defined in Section 2.

Figure 8. Spin density of $I^{-}\cdot A7$ (a) and $H_2PO_3^{-}\cdot A$ (b) with isovalues of 0.002 e^{-}/au^3.

Supplemental material

Near-Threshold Electron Transfer in Anion-Nucleobase Clusters: Does the Identity of the Anion Matter?

Rosaria Cercola,[1] Edward Matthews,[1] and Caroline E. H. Dessent[1]*

1 Department of Chemistry, University of York, Heslington, York, YO10 5DD, UK.

S1 Higher-energy collisional dissociation (HCD) of the $X^-\cdot A$ ($X^-=I^-$ and $H_2PO_3^-$) anionic clusters

Higher-energy collisional dissociation (HCD) was performed to investigate the ground state fragmentation characteristics of the $X^-\cdot A$ ($X^-=I^-$ and $H_2PO_3^-$) anionic clusters. An Orbitrap Fusion Tribrid mass spectrometer (Thermo Fisher Scientific) with an ESI source was employed for these experiments and run in the negative ion mode. The instrument was operated at a flow rate of 5 μL/min. The following settings were used for both clusters: MS1 detector ion trap, MS1 maximum injection time, 100 ms; MS1 automated gain control (AGC) target, 100000; MS2 detector, ion trap; MS2 scan range, 50−600 MS2; AGC target, 100000; MS2 maximum injection time, 100: S-lens RF level, 50 V. The HCD collisional energy was varied between 0 and 46%, and the intensity of the ion in percentage was calculated.

In order to obtain a good cluster production, some parameters were slightly changed when analysing the two clusters $H_2PO_3^-\cdot A$ (a) and $I^-\cdot A$ (b):

a) Spray voltage, 2000 V; sweep gas flow rate, 1; sheath gas flow rate, 40; aux gas flow rate, 5; ion transfer tube temperature, 230°C; vaporizer temperature, 70°C.
b) Spray voltage, 2100 V; sweep gas flow rate, 1; sheath gas flow rate, 45; aux gas flow rate, 17; ion transfer tube temperature, 150°C; vaporizer temperature, 80°C.

$H_2PO_3^-$, $[A-H]^-$ and PO_3^- are produced from $H_2PO_3^-\cdot A$, whilst I^- is the only fragment produced by $I^-\cdot A$.

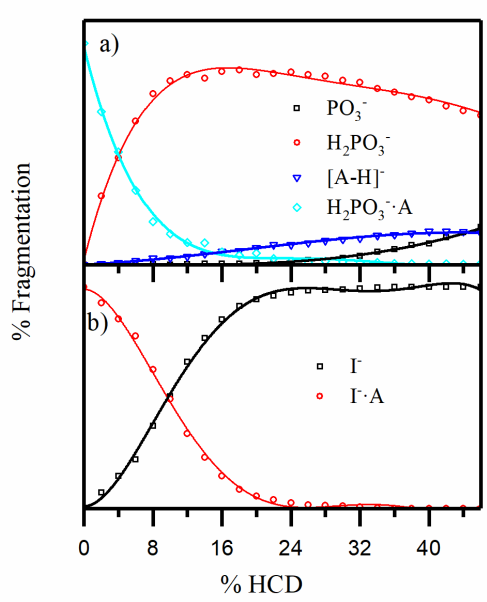

Figure S1: Fragment production curves for $H_2PO_3^-$·A (a) and I^-·A (b) upon HCD between 0 and 46% energy

S2 TD-DFT transitions of $X^{-}\cdot A$ ($X^{-}=I^{-}$ and $H_2PO_3^{-}$)

Figure 3 of the main text shows the TD-DFT spectra of the $X^{-}\cdot A$ ($X^{-}=I^{-}$ and $H_2PO_3^{-}$) clusters. The electronic transitions of the clusters, predicted by TD-DFT, are summarised in tables S1 and S2; including: transition assignments, transition energies and oscillator strengths.

The molecular orbitals involved in the electronic transitions predicted by TD-DFT calculations (performed at the B3LYP/6-311++G(2d,2p)/SDD on I) of the $X^{-}\cdot A7$ ($X^{-}=I^{-}$ and $H_2PO_3^{-}$) clusters are presented in Figures S2 and S3.

According to these calculations, the transitions at 4.86 and 4.90 eV of the $X^{-}\cdot A$ cluster are coupled, more details in Table S1.

Table S1 Calculated TDDFT transition energies and oscillator strengths of the $I^-\cdot A$ (N7H) cluster. Calculations were performed at the B3LYP/6-311++G(2d,2p)/SDD level. Only transitions below 5.5 eV with oscillator strength > 0.005 are listed.

Orbital transitions	ΔE (eV)	f
(1.00)39(n)→40(π*)	3.78	0.0069
(0.79)39(n)→41(σ*)	4.20	0.024
(0.77)38(n)→41(σ*)	4.33	0.040
(0.82)39(n)→42(σ*)	4.40	0.005
(0.79)37(n)→41(σ*)	4.50	0.048
(0.79)38(n)→42(σ*)	4.55	0.010
(0.82)39(n)→44(σ*)	4.60	0.0090
(0.82)37(n)→42(σ*)	4.68	0.0058
(0.82)38(n)→44(σ*)	4.75	0.016
(0.65)36(π)→40(π*)	4.86	0.15
(0.18)37(n)→44(σ*)		
(0.65)37(n)→44(σ*)	4.90	0.027
(0.19)36(π)→40(π*)		
(0.70)35(π)→40(π*)	5.01	0.0064
(0.26)36(π)→41(σ*)		
(0.56)39(n)→45(π*)	5.18	0.091
(0.36)39(n)→46(σ*)		
(0.60)38(n)→45(π*)	5.31	0.064
(0.29)38(n)→46(σ*)		
(0.87)39(n)→47(π*)	5.42	0.011
(0.60)37(n)→45(π*)	5.47	0.13
(0.27)37(n)→46(σ*)		
(0.44)38(n)→46(σ*)	5.50	0.011
(0.18)38(n)→45(π*)		

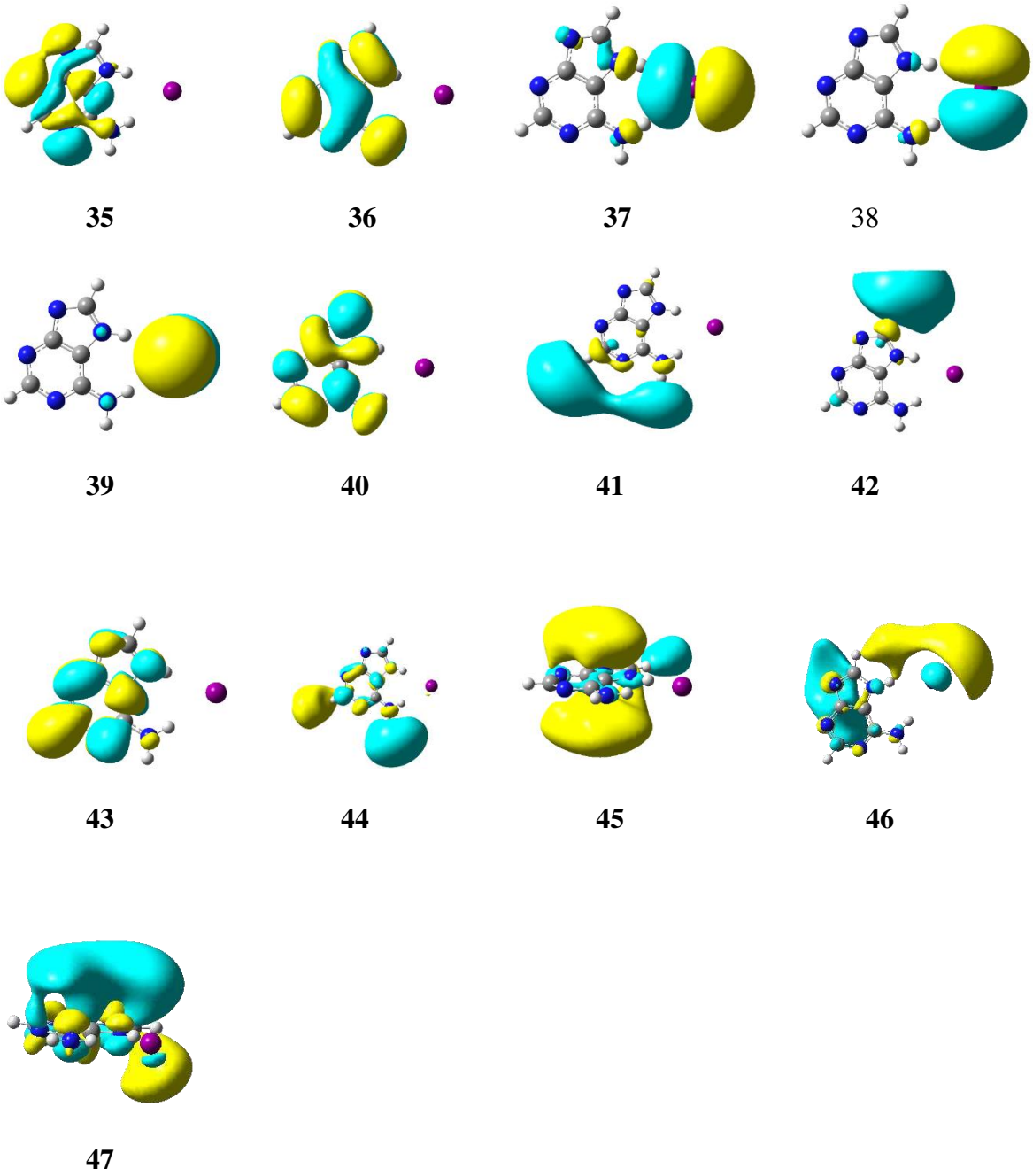

Figure S2: Molecular orbitals of $I^{-}\cdot A$ involved in the transitions predicted by TDDFT calculations between 3.78 – 5.50 eV described in Table S1. The isovalue for each orbital surface is 0.02 e/au^3 .

Table S2 Calculated TDDFT transition energies and oscillator strengths of the $H_2PO_3^- \cdot$A (N7H) cluster. Calculations were performed at the B3LYP/6-311++G(2d,2p) level. Only transitions below 5.8 eV with oscillator strength > 0.005 are listed.

Orbital transitions	ΔE (eV)	f
(0.54)56(π)→58(phosphate σ*)	4.70	0.0052
(0.35)56(π)→59(σ*)		
(0.84)56(π)→57(π*)	4.79	0.15
(0.73)56(π)→62(π*)	5.13	0.0188
(0.29)55(π)→58(phosphate σ*)	5.65	0.0566
(0.67)55(π)→59(σ*)		
(0.57)54(π)→58(phosphate σ*)	5.81	0.0104
(0.21)54(π)→59(σ*)		
(0.46)54(π)→57(π*)	5.85	0.1676
(0.21)56(π)→65(π*)		

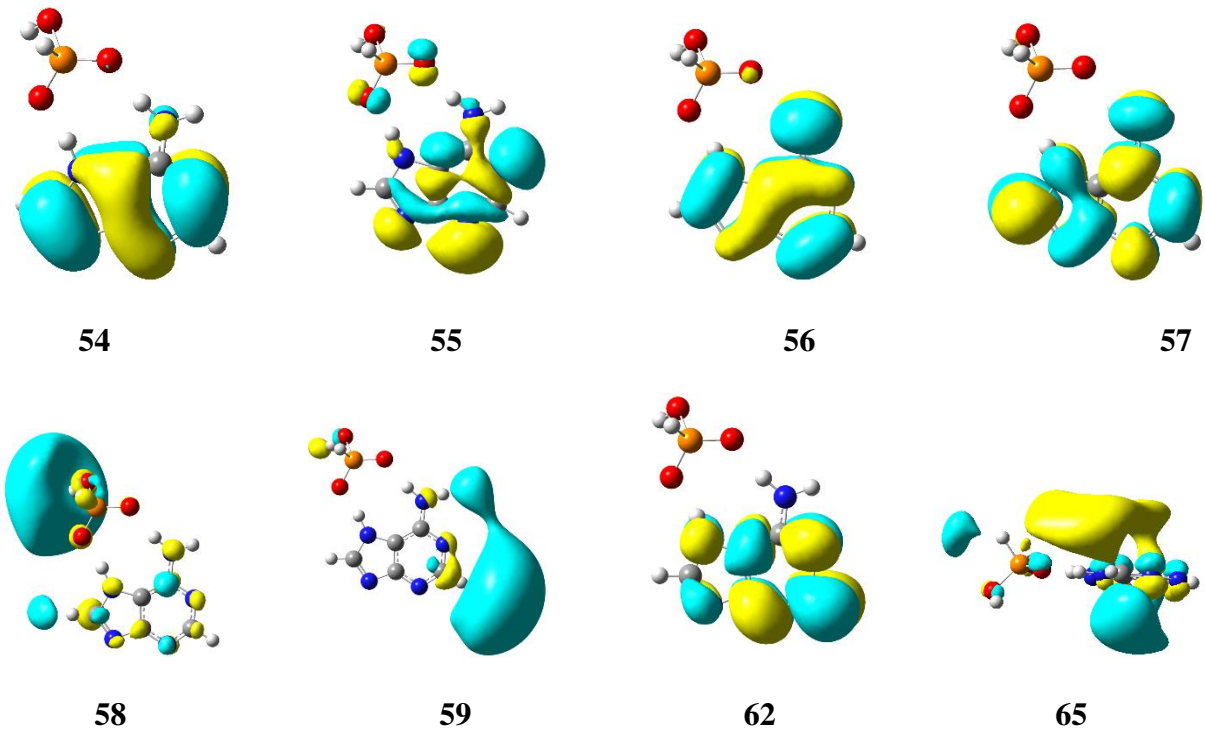

Figure S3: Molecular orbitals of $H_2PO_3^-$·A involved in the transitions predicted by TDDFT calculations between 4.70 – 5.85 eV described in Table S2. The isovalue for each orbital surface is 0.02 e/au^3 .

S3 Photofragment action spectrum of PO_3^- from $H_2PO_3^-\cdot A$

The ion PO_3^- (m/z 79) is produced with a very low cross-section in the photodepletion experiment. Its photofragment action spectrum in shown in Figure S4.

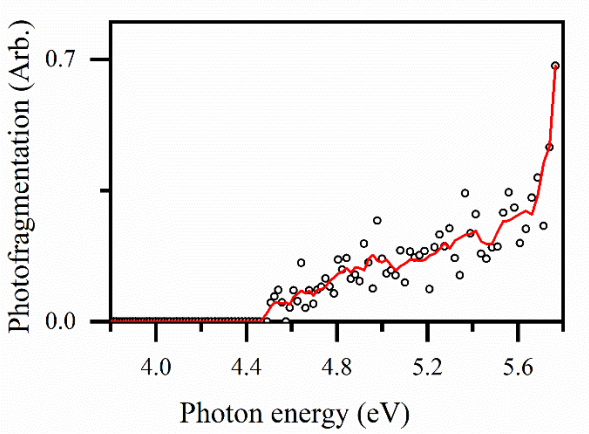

Figure S4: Photofragment action spectrum for PO_3^- that is produced from the $H_2PO_3^-\cdot A$ cluster. The lines are five-point adjacent average of the data points.

S4 Calculated Dipole Moments of $X^-\cdot A$ ($X^-=I^-$ and $H_2PO_3^-$)

Cluster	**MP2 Dipole Detached**[a] Debye	**MP2 Dipole Ground State** Debye
$I^-\cdot A7$	8.80	1.40
$I^-\cdot A9$	3.71	9.02
$I^-\cdot A3$	5.41	7.95
$H_2PO_3^-\cdot A7$	5.88	1.73
$H_2PO_3^-\cdot A9$	14.8	6.09
$H_2PO_3^-\cdot A3$	14.5	4.79

a Vertical dipole moments